

# Neutron capture $^{128}\text{Xe}$ and $^{129}\text{Xe}$ in the San Juan mass of the Campo del Cielo IAB iron meteorite: Evidence for a high fluence of thermalized neutrons

O. PRAVDIVTSEVA <sup>\*1</sup>, M. E. VARELA <sup>2</sup>, A. MESHNIK<sup>1</sup>, A. J. CAMPBELL<sup>3</sup>, M. SAAVEDRA<sup>2</sup>, and D. TOPA<sup>4</sup>

<sup>1</sup>Laboratory for Space Sciences and Physics Department, Washington University, CB1105, Saint Louis, Missouri 63130, USA

<sup>2</sup>ICATE (CONICET-UNSJ), Avenida España 1512 sur, San Juan J5402DSP, Argentina

<sup>3</sup>Department of the Geophysical Sciences, University of Chicago, 5734 S. Ellis Ave., Chicago, Illinois 60637, USA

<sup>4</sup>Central Research Laboratories, Natural History Museum, Burgring 7, Vienna 1010, Austria

\*Corresponding author. E-mail: olga@physics.wustl.edu

(Received 27 February 2021; revision accepted 31 May 2021)

**Abstract**—The petrographic study of the San Juan A2 polished section demonstrated textural and compositional similarities with the Campo del Cielo IAB iron meteorite, with trace element abundances in metal following the pattern of bulk Campo del Cielo. Xenon, neon, and helium isotopic compositions have been measured in radial graphite rims, massive graphite inclusions, fine-grained graphite aggregates, cliftonite, and platy graphite. Two silicate inclusions and two areas of metal were also analyzed.  $^3\text{He}/^4\text{He}$  versus  $^4\text{He}/^{21}\text{Ne}$  data for San Juan metal plot next to the values reported for the El Taco fragment of Campo del Cielo, supporting San Juan being a part of the Campo del Cielo meteorite shower. Based on the Ne isotopic composition of its components, and the observed correlation between  $^{128}\text{Xe}$  and  $^{129}\text{Xe}$ , the San Juan A fragment of Campo del Cielo was well shielded from the primary galactic cosmic ray high-energy irradiation. Its size allowed the secondary neutrons to be fairly well thermalized, receiving an equivalent (normalized to the research reactor with highly thermalized neutron spectrum) fluence of thermal and epithermal neutrons of  $6.6 \times 10^{17} \text{ n cm}^{-2}$ . Considering  $1.8 \times 10^8$  years single-stage and constant exposure geometry irradiation history for Campo del Cielo, and assuming the identical neutron flux spectra for the research reactor and Campo del Cielo, the average thermal equivalent neutron flux for San Juan is about  $1.2 \times 10^2 \text{ n cm}^{-2} \text{ s}^{-1}$ . Xe isotopic composition in the radial graphite rims and platy graphite shows evidence of live  $^{129}\text{I}$  in San Juan and is consistent with a mixture of iodine-derived and tellurium-derived Xe.

## INTRODUCTION

Galactic cosmic rays (GCR)–induced effects provide a means to study the history of meteorites as small objects in space or in the top few meters of their parent body. Most important are cosmogenic nuclides, produced by interactions of primary and secondary cosmic ray particles with target atoms. Interactions with high-energy neutrons and protons usually result in spallogenic nuclides of a lower mass than the original target. Neutron capture of thermal ( $<0.6 \text{ eV}$ ) or epithermal (up to hundreds of eV) secondary neutrons produces heavier nuclides.

Cosmogenic  $^{128}\text{Xe}$  produced by capture of low-energy neutrons on  $^{127}\text{I}$  has been observed in Allende CAIs (Göbel et al. 1982) in correlation with  $^{129}\text{Xe}$  from the decay of now extinct  $^{129}\text{I}$  ( $t_{1/2} = 15.7 \text{ Ma}$ ). While the ratio of the excess amounts of  $^{129}\text{Xe}/^{128}\text{Xe}$  over the trapped Q-Xe value (Busemann et al. 2000) was constant for inclusions from the same Allende specimens, for different specimens, it ranged by a factor of four (Göbel et al. 1982). These cosmogenic excesses on  $^{128}\text{Xe}$  were accompanied by excesses on  $^{80,82}\text{Kr}$  and  $^{36}\text{Ar}$  due to low energy neutron capture on Br and Cl. The ratio of the specific excesses  $^{36}\text{Ar}/^{128}\text{Xe}$  as well as  $^{80}\text{Kr}/^{82}\text{Kr}$  indicated that no more than ~20% of the

neutrons were thermal. Similar thermal neutron capture effects for Xe and Kr were observed recently in two aliquots of the Allende CAI Curious Marie (Pravdivtseva et al. 2020). One of these aliquots was irradiated with well-thermalized neutrons at the Missouri University Research Reactor (MURR) in order to convert  $^{127}\text{I}$  into  $^{128}\text{Xe}$  for the I-Xe study. The difference in  $^{129}\text{Xe}/^{128}\text{Xe}$  between two studied Curious Marie aliquots suggested MURR equivalent GCR fluence of  $\sim 10^{16}$  thermal neutrons per  $\text{cm}^2$ . Many samples of lunar regolith soils displayed  $^{128}\text{Xe}$  excesses, but for the most part, they were modest and statistically insignificant (Pepin et al. 1995).

For the silicates in the El Taco fragment of the Campo del Cielo IAB iron meteorite, cosmogenic  $^{127}\text{I}$  (n, $\gamma$ )-produced  $^{128}\text{Xe}$  and radiogenic  $^{129}\text{Xe}$  were released together, with the same  $^{129}\text{Xe}/^{128}\text{Xe}$  ratio in nominal olivine, pyroxene, and feldspar indicating closure of the I-Xe system in pyroxene and feldspar within  $\sim 2$  Ma (Mathew and Begemann 1995). A similar I-Xe age difference of  $1.6 \pm 0.6$  Ma was observed for neutron-irradiated diopside and oligoclase from Campo del Cielo (Pravdivtseva et al. 2013). The I-Xe systematics in these silicates were consistent with formation by separate impact events at different locations and depths on a porous initial chondritic IAB parent body. These events were followed by a larger scale catastrophic collision that caused a breakup and reassembly of the debris, but did not reset the I-Xe ages dating the earlier impacts. This conclusion was in line with complex characteristics of IABs that do not fit into any simple formation scenario. The IAB iron meteorites (Wasson et al. 1980; Kracher 1982; Choi et al. 1995; Benedix et al. 2000; Wasson and Kallemeyn 2002; Ruzicka 2014) contain chondritic silicates closely related to carbonaceous chondrites with plagioclase contents that vary from clast to clast. Previous Xe isotopic composition studies of IAB iron meteorites focused on silicates known to contain abundant primordial noble gases and on bulk graphite (Podosek 1970; Neimeyer 1979; Mathew and Begemann 1995; Takeda et al. 2000; Maruoka et al. 2001; Bogard et al. 2005; Vogel and Renne 2008).

This work was motivated by the diverse morphology of graphite inclusions in the San Juan A2 fragment of Campo del Cielo and by the potential information on the complex early history of IAB iron meteorites they might preserve. To study these inclusions individually, we used *in situ* laser extraction and measured isotopic composition of He, Ne, and Xe.

## SAMPLES AND ANALYTICAL TECHNIQUES

A small ( $\sim 760$  g) and a large ( $\sim 53$  kg) piece of meteoritic iron were found in the San Juan province of

Argentina and were named San Juan A and B, respectively. A preliminary investigation of the metal of San Juan A revealed that it is a part of the Campo del Cielo IAB iron meteorite shower (Kurat et al. 2002). The small San Juan A mass of Campo del Cielo is a coarse octahedrite which has three angular silicate inclusions of up to about  $1 \text{ cm}^2$  in size. Three polished sections (named San Juan A1, A2, and A3) of the exposed silicate inclusions show that they consist of olivine, graphite, orthopyroxene, plagioclase, clinopyroxene, and small amounts of metal and sulfide. For the present study, the San Juan A2 sample from the collection of the Vienna Museum of Natural History (inventory number: NHMV-O333, Fig. 1) was selected based on the morphology of the graphite types (e.g., presence of graphite rims, platy and massive graphite) as well as their textural relationships with silicates and metal (Fig. 1b).

The polished section of San Juan A2 was studied by optical microscopy for the petrographic characteristics of the constituent phases (e.g., silicate inclusions, metal, sulfide, troilite). Major element chemical compositions of constituent phases were obtained with a JEOL 6400 and a JEOL JSM-6610 scanning electron microprobe (NHM, Vienna) operated at a sample current of 1 nA and an acceleration voltage of 15 kV and with an ARL-SEMQ (ICATE), a SX100 (Institute of Geological Sciences, University of Vienna), and a JEOL JXA-8530F FE (NHM, Vienna) electron microprobes. Electron microprobe analyses were performed using 15 kV acceleration potential and a beam current of 20 nA. Analyses by the JEOL JXA-8530F FE were performed using 1–2  $\mu\text{m}$  beam diameter and a counting time of 10 s for peak and 5 s for background. The following synthetic compounds  $\text{Al}_2\text{O}_3$ ,  $\text{Cr}_2\text{O}_3$ ,  $\text{TiO}_2$ ,  $\text{NiO}$ , and  $\text{NaCl}$  were used as standards for Al, Cr, Ti, and Na, respectively. Natural minerals tephroite,  $\text{Mn}_2\text{SiO}_4$ , troilite  $\text{FeS}$ , and Marjalahti olivine ( $\text{Mg}, \text{Fe})_2\text{SiO}_4$  were used as standards for Mn, Fe, and Mg, respectively.

The LA-ICP-MS analyses of metal were performed following the procedures of Campbell et al. (2001). A CETAC LSX-200 laser ablation peripheral was used with a magnetic sector ICP mass spectrometer, the Finnigan Element<sup>TM</sup>. Each analysis on the sample produced a pit 25–100  $\mu\text{m}$  in diameter and 15–25  $\mu\text{m}$  deep. Some analyses rastered the laser across the sample during collection. The isotopes  $^{31}\text{P}$ ,  $^{57}\text{Fe}$ ,  $^{59}\text{Co}$ ,  $^{60}\text{Ni}$ ,  $^{63}\text{Cu}$ ,  $^{69}\text{Ga}$ ,  $^{74}\text{Ge}$ ,  $^{95}\text{Mo}$ ,  $^{101}\text{Ru}$ ,  $^{103}\text{Rh}$ ,  $^{182}\text{W}$ ,  $^{185}\text{Re}$ ,  $^{192}\text{Os}$ ,  $^{193}\text{Ir}$ ,  $^{195}\text{Pt}$ , and  $^{197}\text{Au}$  were monitored during the measurements. Instrumental sensitivity factors for each isotope relative to  $^{57}\text{Fe}$  were determined from metal standards which have known concentrations of the elements of interest (Campbell

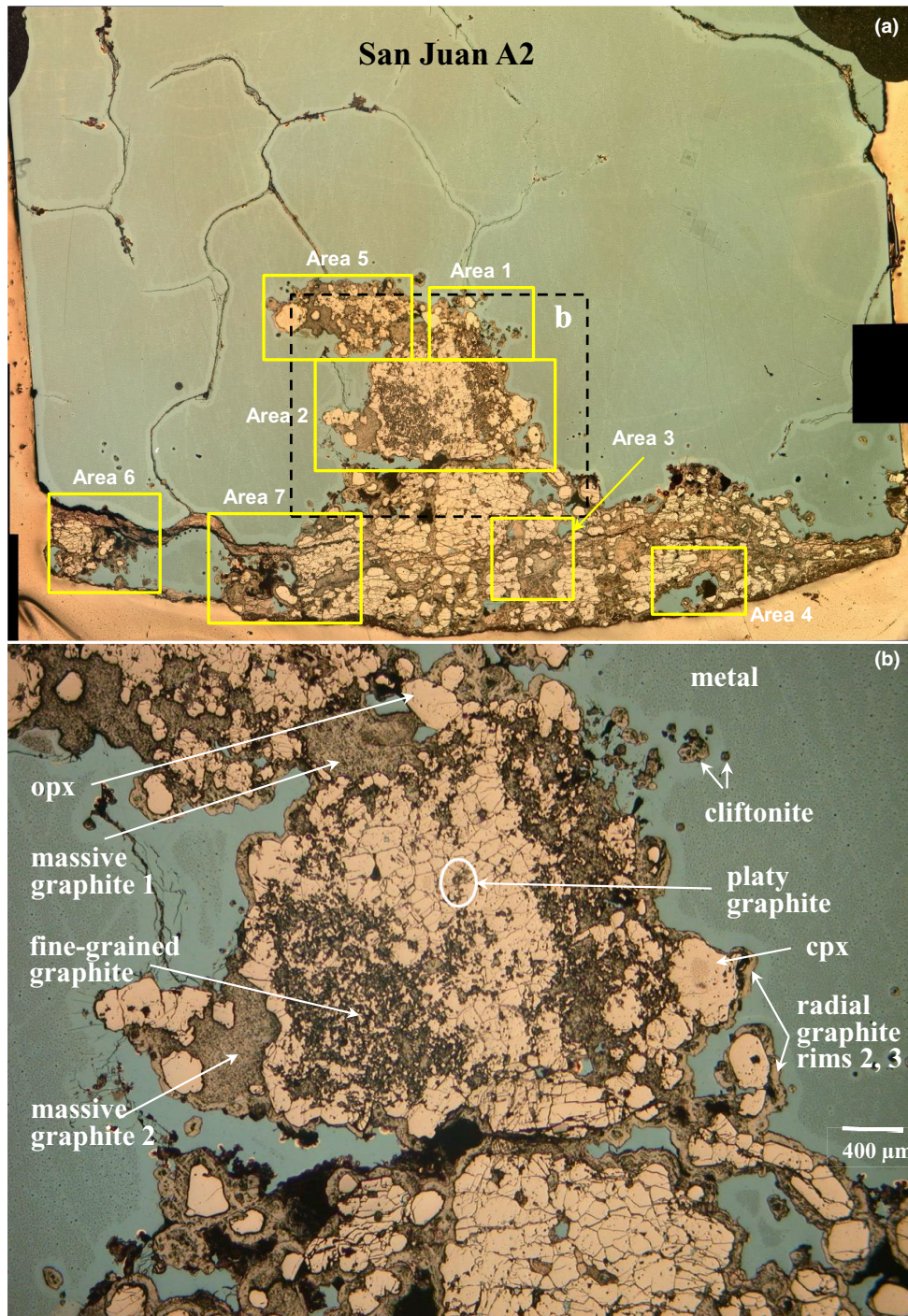


Fig. 1. a) Polished thick section of San Juan A2 (inventory number: NHMV-O333). Outlined by yellow solid lines are the seven studied areas. Outlined by a dashed line is the area enlarged in (b) where some of the analyzed mineral phases are marked. Platy graphite, circled in (b), was too small for the noble gas analyses; instead a larger graphite plate from Area 3 was analyzed. Radial graphite rim 1 is located in Area 5. opx = orthopyroxene; cpx = clinopyroxene.

et al. 2001); these standards included the iron meteorites Hoba IVB (Co, Ni, PGEs, Re, Au), Filomena IIA (Ga, Ge, W), and the NIST SRM 1263a

(P, Cu, Mo, W, Au). The corrected intensities were converted to elemental abundances by normalization to  $[\text{Fe}] + [\text{Co}] + [\text{Ni}] + [\text{P}] = 100 \text{ wt\%}$ .

Xenon, neon, and helium isotopic compositions have been measured in radial graphite rims surrounding silicates, massive graphite inclusions, fine-grained graphite aggregates, cliftonite (octahedral form of graphite) inclusions, and platy graphite. Two silicate inclusions were also analyzed, as well as two areas of metal. For the noble gas analyses, we used *in situ* laser extraction to ablate selected areas of the sample preserving the polished section for future studies. The polished section was cut from the mounting epoxy, cleaned with methanol and acetone, and placed into the laser extraction cell with a sapphire viewport. The cell was mounted on the computer-controlled X-Y Newport stage. An acoustically Q-switched Nd-YAG laser (1064 nm) generated a 3 mm beam with an average power of 6 W. The beam was reflected by 45° dichroic mirror and focused on a 15 μm spot using antireflection-coated planar-convex lens. The software, written in Lab-View, allowed moving the stage along the customized paths and shapes including several basic ones (Fig. 2) while firing the laser on and off, providing ~5 μm overlapping of the adjoining laser pulses. The total pressure of gas released during the laser extraction was monitored by an absolute pressure sensor (MKS Baratron, 0.1 Torr range, held at 100 °C). The number of the extracted layers in the analyzed mineral phases varied from 2 to 6 and was selected based on the total pressure of the extracted gases. Released gases were sequentially cleaned from the chemically active components by first exposing them to the hot SAES St707 getter pellets (5 min at 275 °C, following another 5 min at cooling), and then to freshly deposited Ti-films. Xenon was separated from light noble gases using activated charcoal at a temperature of -90 °C for the adsorption of Xe and +165 °C for Xe desorption, maintained within ±1 °C by a two-step PID controller. The He and Ne isotopic compositions were measured first by high-transmission mass spectrometer SuperGnome-S at Washington University, Saint Louis (Meshik and Pravdivtseva 2016). Xenon was analyzed subsequently using optimized detection parameters. Sensitivity was  $1.6 \times 10^{-14}$  cm<sup>3</sup> STP/Hz for He,  $7.2 \times 10^{-15}$  cm<sup>3</sup> STP/Hz for Ne, and  $7.0 \times 10^{-16}$  cm<sup>3</sup> STP/Hz for Xe. Instrumental mass discrimination for neon and xenon was monitored by air standard purified from chemically active gases. The final mass discrimination correction was based on 14 air standard measurements and was ~2%/u for Ne and ~0.1%/u for Xe. Isotopic compositions of He, Ne, and Xe, released by firing the laser into the stainless steel bottom of the extraction cell for 10 s, and then separated and cleaned following the standard protocol, were used for the background corrections.

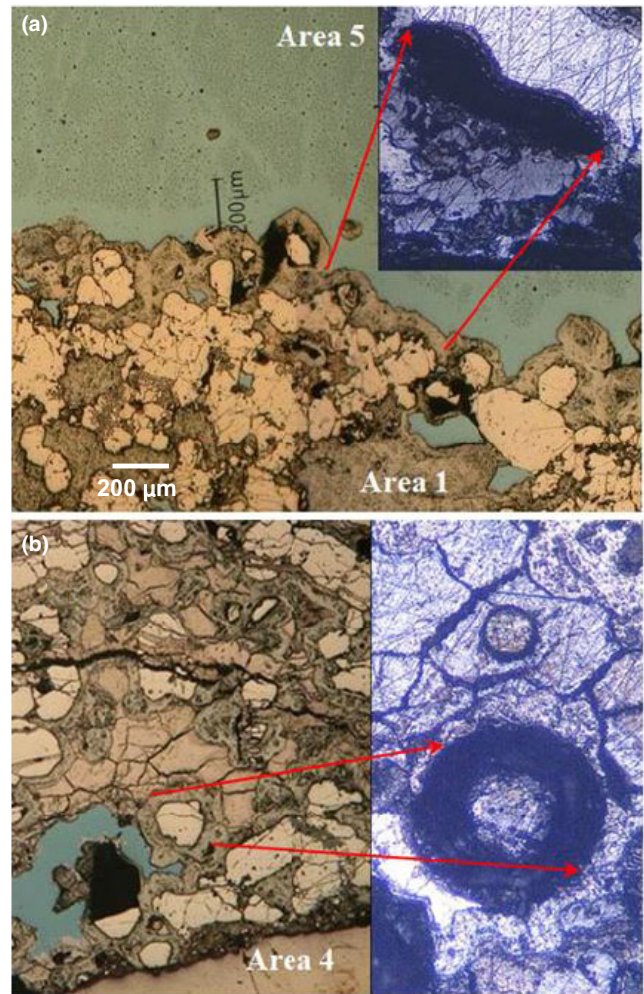


Fig. 2. Selective gas extraction by *in situ* laser ablation. Monochrome inserts are views through the laser microscope after rastering; (a) the ablated section of the radial rim is bordered by metal on the one side and silicates on the other side; (b) circular ablation path around the silicate inclusion. Smaller circular path above is a test run.

## RESULTS

### Petrography and Chemical Composition

The texture of San Juan A2 is coarse granular with grain sizes varying from place to place; and containing magnesian olivine (Fo<sub>94.9</sub>) and orthopyroxene (En<sub>90.6</sub>, Fs<sub>7.7</sub>, Wo<sub>1.7</sub>), albitic plagioclase (An<sub>14.7</sub>), high-Ca pyroxene (En<sub>53</sub>, Fs<sub>3.4</sub>, Wo<sub>43.7</sub>), and graphite (Table 1). The latter is omnipresent inside the silicate inclusion, filling intergranular and interaggregate spaces and covering the inclusion surface (Fig. 1). Cliftonite and multiple intergrowths thereof are abundantly present in kamacite of the octahedrite metal. The latter is

Table 1. Chemical composition of mineral phases from San Juan A2 (mean value of the seven areas, in wt%).

	Plagioclase	SD	Low-Ca Pyx	SD	High-Ca Pyx	SD	Olivine	SD
N	18		64		10		30	
SiO <sub>2</sub>	63.50	0.37	57.40	0.23	50.0	2.5	40.4	0.2
TiO <sub>2</sub>	0.08	0.01	0.25	0.01	0.73	0.05	0.03	0.01
Al <sub>2</sub> O <sub>3</sub>	21.9	0.1	0.26	0.01	1.40	0.84		
Cr <sub>2</sub> O <sub>3</sub>	0.02	0.01	0.36	0.03	1.0	0.4	0.02	0.01
FeO	0.33	0.09	4.56	0.07	3.0	1.0	4.8	0.2
MnO	0.02	0.01	0.51	0.01	0.26	0.03	0.40	0.03
MgO	0.01		37.00	0.17	20.0	1.2	54.4	0.4
CaO	3.13	0.05	0.77	0.05	22.1	0.7		
Na <sub>2</sub> O	10.10	0.14	0.04	0.002	0.6	0.3		
Total	99.09		101.15		100.26		100.02	
Mole percent mineral endmembers								
An	14.65							
Ab	85.35							
Wo			1.68		43.15			
En			90.57		52.98			
Fs			7.75		3.87			
Te							0.38	
Fo							94.9	
Fa							4.67	

SD = standard deviation; Pyx = pyroxene; N = number of analyses; An = anorthite; Ab = albite; Wo = wollastonite; En = enstatite; Fs = ferrosilite; Te = tephroite; Fo = forsterite; Fa = fayalite.

homogeneous and contains 6.3 wt% Ni and 0.46 wt% Co. Troilite is highly abundant in silicate inclusions (Fig. 3a) and can also be found in contact with graphite rims (Fig. 3b). Metal of different occurrences in San Juan A2 is fairly similar with respect to its Ni and Co contents (Table 2). Siderophile trace element contents of the metal are similar, whether the metal is found in the octahedrite, in a metal vein, as embayment in silicate inclusions forming metal islands, or if it is finely dispersed in the graphite (Table 2). The abundances of the siderophile elements in metal having different occurrences are slightly fractionated and like those in Campo del Cielo bulk (Fig. 4). The angular to subrounded shapes of the graphite-chondritic inclusions, their textures, and the chemical composition of silicates and metal indicate that San Juan A is another piece of the Campo del Cielo meteorite shower with trace element abundances of metal following exactly the pattern of bulk Campo del Cielo (Wlotzka and Jarosewich 1977; Jochum et al. 1980; Hoashi et al. 1993; Choi et al. 1995; Benedix et al. 2000; Kurat et al. 2002; Ruzicka 2014).

### Noble Gas Isotopic Composition

The He, Ne isotopic compositions in the laser-rastered areas are combined in Table 3 and the isotopic composition of Xe in Table 4. Most of the rastered areas had complex shapes, dictated by outline

of the analyzed mineral phase. Although the surface area and the number of excavated layers for each raster are known, the amount of degassed material in the rasters could not be accurately estimated. With each consecutive raster, the shape of the excavated area was smaller and more distorted. In addition, while some material was evaporated and deposited on the viewport of the laser cell and the sample surface, a fraction of it was redeposited on the freshly rastered surface. Finally, we could not rule out the degassing from the material adjoined to the actual laser pit. Therefore, we do not report noble gas concentration values for San Juan A2 metal, graphites, and silicates. Instead, ion count rates for each sample are shown in Tables 3 and 4. The count rates for each mineral phase roughly correspond to the volume of excavated areas.

Ratios of spallogenic isotopes  $^3\text{He}/^4\text{He}$  versus  $^4\text{He}/^{21}\text{Ne}$  in analyzed areas are shown in Fig. 5 relative to the published data for iron meteorites (Hintenberger and Wänke 1963; Nyquist et al. 1967; Voshage et al. 1983; Lavielle et al. 1999; Maruoka et al. 2001). Isotopic composition of neon from different mineral phases (Fig. 6) is consistent with a mixture of atmospheric and spallogenic components (Basford et al. 1973; Busemann et al. 2000).

The Xe isotopic composition in San Juan A2 silicates and graphite inclusions is a mixture of two major components, air and iodine-derived Xe (Fig. 7).

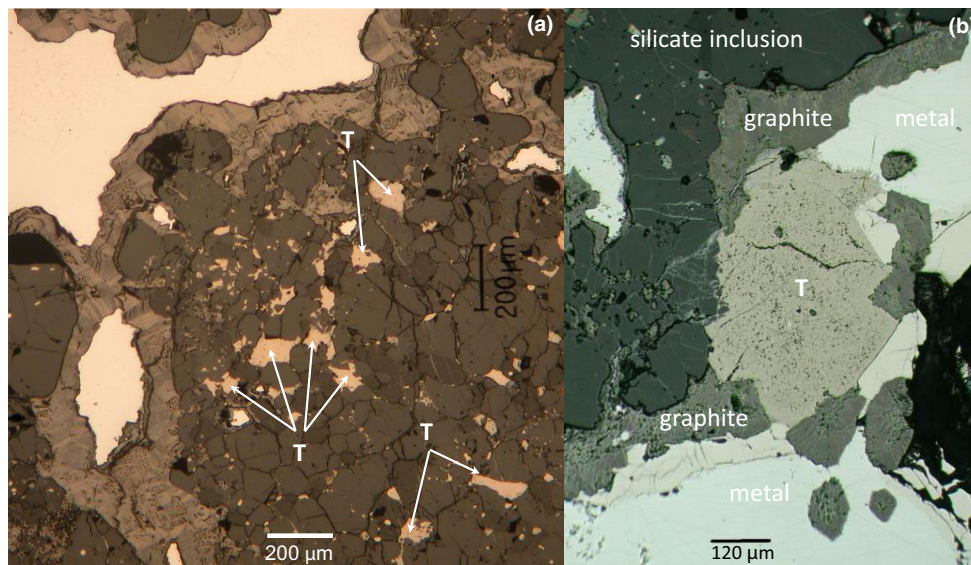


Fig. 3. Optical image showing the abundant presence of troilite (T) in the silicate inclusion (a) and in contact with the graphite rim (b) in a polished section from the San Juan A mass of Campo del Cielo (IAB).

Table 2. Representative LA-ICP-MS analyses of metal from San Juan A2 (in ppm, with  $2\sigma$  errors).

	Metal	$2\sigma$	Island metal	$2\sigma$	Metal in graphite	$2\sigma$	Metal vein	$2\sigma$
W	1.00	0.18	1.64	0.2	1.59	0.2	1.05	0.22
Mo	7.35	1.13	9.1	0.9	8.43	0.85	5.86	1.3
Re	0.27	0.08	0.42	0.07	0.44	0.07	0.28	0.08
Os	3.57	0.42	5.59	0.44	5.31	0.42	3.33	0.45
Ir	2.96	0.28	4.86	0.37	4.47	0.35	2.86	0.37
Ru	5.00	0.6	6.89	0.66	5.96	0.6	4.56	0.8
Pt	5.32	0.52	9.03	0.73	7.85	0.65	5.60	0.76
Co	4795	346	5126	338	5023	332	4565	385
Ni	55,749	4893	60,881	4018	63,182	4170	55,379	6566
Pd	2.16	0.4	3.41	0.42	3.44	0.42	2.32	0.55
Au	1.22	0.16	1.75	0.18	1.66	0.17	1.52	0.22
Cu	96	11	118	7.9	107	7.2	106	15.6
Ge	412	33	399	26.5	367	24.4	459	41.5
Ga	80	7.8	92	7.8	93	6.2	82	7

References: Metal vein: Scan across a vein. Mean value of 35 points (each point represents average over 27.5  $\mu\text{m}$  of laser beam travel).

None of the samples showed excesses due to either spallation on Ba/REE or U fission (Fig. 7; Table 4).

## DISCUSSION

### Helium and Neon

Ratios of spallogenic He and Ne isotopes (Fig. 5) follow the correlation trend defined by the published data for iron meteorites where  $^3\text{He}/^4\text{He}$  values decrease and  $^4\text{He}/^{21}\text{Ne}$  values increase with the size of meteorite. Data points for San Juan metal are similar to the values reported for the El Taco fragment of Campo del Cielo

(Nyquist et al. 1967), supporting San Juan being a part of the Campo del Cielo meteorite shower.

Neon isotopic composition in analyzed mineral fractions of San Juan (Fig. 6) is consistent with a mixture of spallogenic and air (introduced by cutting and polishing) components. Most data points fall on a dotted line connecting atmospheric neon composition and the two data points for orthopyroxene and fine-grained graphite with the highest  $^{21}\text{Ne}$  enrichment. The  $^{21}\text{Ne}/^{22}\text{Ne}$  values in two San Juan A2 silicates studied here range from 0.96 to 1.07, with an average value of 1.04, indicating irradiation in a large body at a large shielding depth. The pre-atmospheric size of Campo del

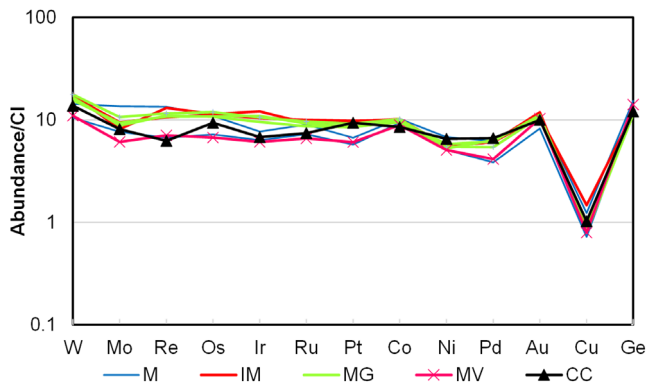


Fig. 4. CI-normalized (Lodders et al. 2009) elemental abundances in metal from San Juan A2 compared to Campo del Cielo bulk composition. M = octahedrite; IM = metal islands occurring as embayment in silicate inclusions; MG = metal in graphite; MV = metal vein; CC = Campo del Cielo.

Cielo was estimated from the concentration of long-lived cosmogenic  $^{36}\text{Cl}$  (Lieberman et al. 2002). With a radius larger than 3 m, it might be one of the largest iron meteorites to have been recovered (Ruzicka 2014). A flux of secondary neutrons increases with depth, making  $^{21}\text{Ne}$  production by the reaction  $^{24}\text{Mg}(n,\alpha)^{21}\text{Ne}$  important. This is reflected in the higher  $^{21}\text{Ne}/^{22}\text{Ne}$  value for orthopyroxene that is richer in MgO compare to clinopyroxene (both red symbols, Fig. 6). Data points for both analyzed massive graphite inclusions fall slightly below the correlation line, although within  $2\sigma$ , suggesting a possible contribution from the Ne-HL component carried by nanodiamonds (Huss and Lewis 1994).

## Xenon

The trapped component in the studied mineral phases of San Juan A2 is atmospheric in composition (Ozima and Podosek 1983) (Fig. 7). The detailed Xe isotopic study of silicates and graphite from El Taco, another fragment of Campo del Cielo (Mathew and Begemann 1995), revealed two distinctly different trapped planetary noble gases. While Xe in silicates was a mixture of atmospheric and ureilite Xe (Göbel et al. 1978), in graphite and schreibersite, it was a mixture of atmospheric and a previously unknown component, named by the authors El Taco xenon. Xenon was released by stepwise heating; the atmospheric component dominated at low temperatures for all studied samples. In graphite from the Bohumilitz IAB iron meteorite, trapped Xe was a mixture of the air, El Taco, and Q components (Maruoka et al. 2001). In this later work, two graphite samples were studied: one as a bulk and another after removal of silicates and metal by

Table 3. He and neon in the mineral phases of San Juan A2 after correction for blank. Stated errors are statistical  $1\sigma$ .

Sample	He count rate (Hz)	$^3\text{He}/^4\text{He}$	He count rate (Hz)	$^{21}\text{Ne}/^{20}\text{Ne}$	$^{22}\text{Ne}/^{20}\text{Ne}$
Met1	10,392	0.2482 0.0064	1039	0.04994 0.00057	0.1545 0.0089
Met2	22,068	0.2481 0.0037	923	0.1168 0.0018	0.199 0.011
Rim1	15,884	13.46 0.41	1672	0.4170 0.0026	0.4581 0.0067
Rim2	8867	12.68 0.71	1158	0.3808 0.0039	0.4324 0.0085
Mas1	—	n.d.	656	0.1652 0.0036	0.286 0.012
Mas3	1719	4.7 4.6	1076	0.01053 0.00041	0.1209 0.0086
Fgr1	56,901	15.00 0.18	8303	0.4504 0.0010	0.4881 0.0019
Fgr2	82,391	13.17 0.15	14,876	0.3484 0.0010	0.3997 0.0012
Fgr3	28,847	14.56 0.25	3524	0.8778 0.0027	0.8542 0.0044
opx	57,218	6.01 0.12	2375	0.7304 0.0027	0.7787 0.0053
cpx	38,187	15.27 0.21	2652	0.8762 0.0049	0.8560 0.0065
Clift.	6002	14.3 1.1	866	0.5007 0.0056	0.515 0.012
Platy	5201	4.9 1.1	1932	0.0122 0.0003	0.1149 0.0046

etching. In the bulk sample, ~96% of trapped Xe was atmospheric, 92% of it released in the first 800 °C extraction. About 50% of trapped Xe was atmospheric in the etched graphite sample. It is clear that in San Juan A2 samples studied *in situ*, the atmospheric component will dominate other less abundant ones. And since noble gases in this work were released at melting of the samples, these components cannot be resolved as it was done in the previous stepwise heating experiments (Mathew and Begemann 1995; Maruoka et al. 2001).

When plotted as  $^{129}\text{Xe}/^{132}\text{Xe}$  versus  $^{128}\text{Xe}/^{132}\text{Xe}$ , data points representing silicates, fine-grained graphites, and cliftonites (solid symbols, Fig. 8) form a well-defined correlation line with the slope of  $16.3 \pm 0.8$ . Fine-grained graphite in San Juan A2 is intermixed with silicates. Thus, Xe in the fine-grained graphite extractions most likely is from both, fine-grained graphite and silicates, which are a mixture of olivine, pyroxene, and plagioclase. Based on the Ne isotopic composition of the three analyzed fine-grained graphite

Table 4. Xenon in mineral phases of San Juan A2 after correction for blank. Stated errors are statistical  $1\sigma$ . Isobaric interferences, blank contributions, and instrumental mass discrimination were considered as systematical errors, they were corrected for and correlated error propagated.

Sam	$^{132}\text{Xe}$ count rate (Hz)	$^{132}\text{Xe} \equiv 100$							
		$^{124}\text{Xe}$	$^{126}\text{Xe}$	$^{128}\text{Xe}$	$^{129}\text{Xe}$	$^{130}\text{Xe}$	$^{131}\text{Xe}$	$^{134}\text{Xe}$	$^{136}\text{Xe}$
Met	256	0.416	0.288	7.33	101.7	15.35	79.3	38.44	33.66
		0.045	0.048	0.24	1.1	0.408	1.2	0.89	0.65
Rim1	367	0.361	0.317	7.32	101.85	15.13	78.1	38.89	32.56
		0.022	0.033	0.17	0.96	0.28	1.1	0.65	0.67
Rim2	367	0.421	0.333	8.13	120.77	15.71	79.2	39.54	32.69
		0.032	0.028	0.15	0.97	0.23	1.2	0.62	0.48
Rim3	237	0.334	0.333	7.74	118.9	14.87	82.1	39.10	33.04
		0.055	0.042	0.19	1.3	0.49	1.1	0.65	0.58
Mas1	1016	0.364	0.333	7.612	110.33	15.17	78.84	38.86	32.64
		0.019	0.016	0.094	0.78	0.19	0.57	0.31	0.34
Mas2	381	0.411	0.321	7.75	110.6	15.14	80.06	38.04	32.56
		0.033	0.042	0.15	1.1	0.21	0.91	0.54	0.61
Mas3	496	0.421	0.352	7.34	106.62	15.32	79.23	39.61	33.30
		0.030	0.031	0.11	0.95	0.20	0.59	0.60	0.36
Fgr1	6675	0.3739	0.3559	7.583	107.65	15.136	78.84	38.73	32.93
		0.0092	0.0069	0.045	0.31	0.059	0.27	0.17	0.16
Fgr2	8725	0.351	0.3620	8.037	114.11	15.353	79.43	39.38	33.11
		0.012	0.0051	0.066	0.40	0.096	0.26	0.21	0.11
Fgr3	5191	0.3725	0.3431	8.014	113.04	15.123	78.81	38.56	33.01
		0.0082	0.0071	0.048	0.28	0.089	0.30	0.16	0.17
Fgr4	646	0.337	0.343	10.13	150.8	14.90	78.8	37.95	32.19
		0.024	0.025	0.15	1.1	0.21	1.2	0.43	0.48
opx	321	0.397	0.340	11.01	160.3	15.47	79.36	40.04	32.50
		0.039	0.031	0.26	1.4	0.31	0.98	0.74	0.63
cpx	252	0.448	0.310	8.71	125.26	15.66	78.2	38.18	32.82
		0.052	0.038	0.27	0.96	0.33	1.1	0.76	0.75
Clift.	116	0.396	0.311	7.93	114.1	14.37	78.8	37.6	33.21
		0.066	0.056	0.27	2.0	0.54	1.7	1.0	0.91
Platy	177	0.372	0.323	7.60	119.0	15.66	79.4	37.51	34.28
		0.055	0.043	0.23	1.6	0.50	1.1	0.82	0.86

Met = metal; Rim = radial graphite rim; Mas = massive graphite; Fgr = fine-grained graphite; opx = orthopyroxene; cpx = clinopyroxene; Clift = cliftonite; Platy = platy graphite.

inclusions, the major contributor of radiogenic Xe in fine-grained silicates is orthopyroxene. Analyzed cliftonite (solid square) was surrounded by metal, making contribution from silicates unlikely. The correlation line is essentially the I-Xe isochron, indicating that the I-Xe system in silicates, cliftonite, and fine-grained graphites in San Juan A2 closed within 2 Ma, consistent with previous observations for silicates in the El Taco fragment of Campo del Cielo (Mathew and Begemann 1995).

The unknown neutron fluence and spectrum evidently prevent the time of closure of the I-Xe system in San Juan A2 from being obtained. However, we can estimate the thermal neutron equivalent fluence received by this sample from the slope of the correlation line in Fig. 7. In our previous studies of Campo del Cielo silicates (Pravdivtseva et al. 2013), we determined

closure times of the I-Xe system in two individual grains, diopside and oligoclase, extracted from the metal. To convert  $^{127}\text{I}$  into  $^{128}\text{Xe}$ , both grains and the absolute age standard Shallowater were irradiated with thermal neutrons at the MURR to the fluence of  $2 \times 10^{19}$  neutrons per  $\text{cm}^2$ . Xe isotopic compositions were measured in stepwise heating experiments. The ratios of the excess amounts of  $^{129}\text{Xe}/^{128}\text{Xe}$  were constant for both grains from  $\sim 1300$  °C up to melting. Plotted as  $^{129}\text{Xe}/^{132}\text{Xe}$  versus  $^{128}\text{Xe}/^{132}\text{Xe}$ , these ratios defined correlations with the slopes of  $0.5173 \pm 0.0038$  for diopside and  $0.5547 \pm 0.0153$  for oligoclase, corresponding to an age difference of 1.6 Ma (Pravdivtseva et al. 2013). Assuming the I-Xe system in all silicates in Campo del Cielo and its fragments closed within this 1.6 Ma interval, the difference in thermal neutron fluences (GCR exposure versus reactor

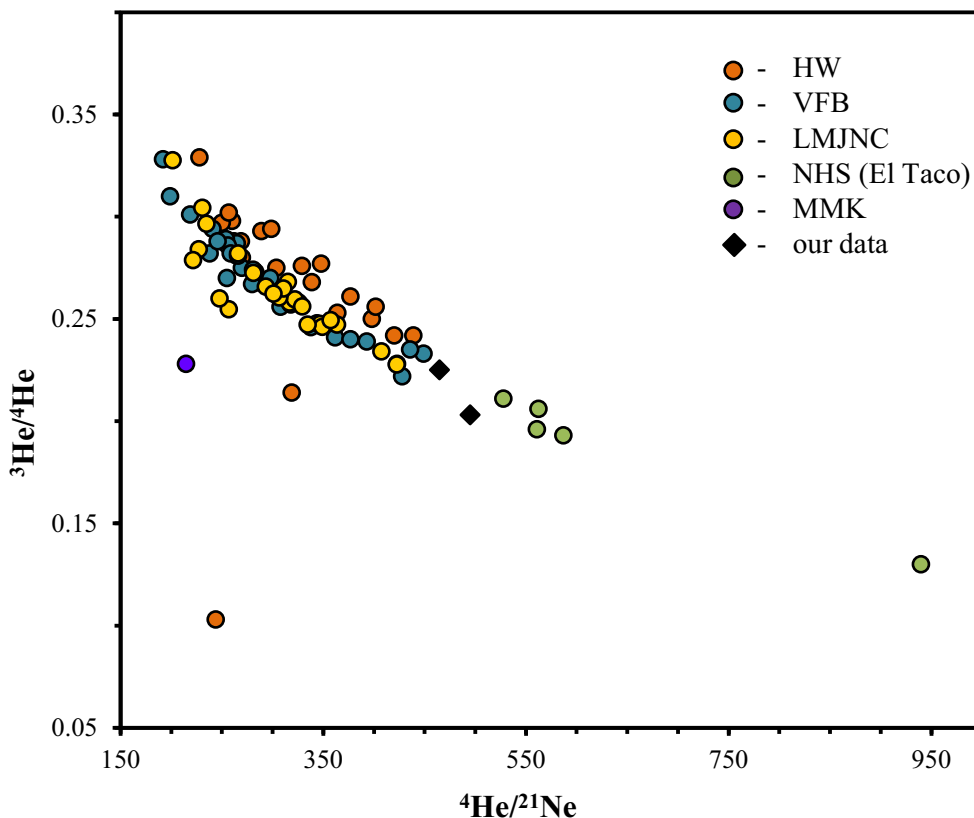


Fig. 5. Ratios of spallogenic isotopes  $^3\text{He}/^4\text{He}$  versus  $^4\text{He}/^{21}\text{Ne}$  in two metal samples of San Juan A2 (black symbols) are shown together with published data for iron meteorites. Letters correspond to the reference: HW—Hintenberger and Wänke (1963); VFB—Voshage et al. (1983); LMJNC—Lavielle et al. (1999); MMK—Maruoka et al. (2001); NHS—Nyquist et al. (1967).

irradiation) can be derived from the difference in the slopes of the San Juan A2 and Campo del Cielo silicates' correlation lines. Based on this estimation, the San Juan A2 mineral phases studied here experienced 29–32 times lower fluence than Campo del Cielo silicates, or about  $6.5 \times 10^{17}$  thermal equivalent neutrons per  $\text{cm}^2$ , compared to values reported for lunar soils (Burnett et al. 1972; Curtis and Wasserburg 1975) and large chondrites (Bogard et al. 1995). Campo del Cielo apparently experienced a simple single-stage irradiation history, without any mechanical damage (constant exposure geometry) for more than 180 Ma (Honda et al. 2009). Assuming the neutron flux spectra are identical for MURR and Campo del Cielo (certainly not true but good for an estimate), the average thermal equivalent neutron flux for these fragments is about  $1.2 \times 10^2 \text{ n cm}^{-2} \text{ s}^{-1}$ .

Radial rims, platy graphite, and massive graphite have higher  $^{129}\text{Xe}/^{128}\text{Xe}$  ratios with corresponding data points falling above the isochron, although the massive graphite data points are within 2 sigma of

correlation line. Rims are closely associated with silicates, while massive graphite with lower  $^{129}\text{Xe}$  excesses and platy graphite with the highest  $^{129}\text{Xe}$  excess over the iodine-derived  $^{129}\text{Xe}$  are less so (all shown as open symbols, Fig. 7). Thus, the apparent extra  $^{129}\text{Xe}$  in rims, large graphite plate, and massive graphites cannot be explained by contribution from silicates due to preferential accumulation of iodine in silicates at the time of silicate + metal mixing and graphite exsolution from metal. Besides, the same  $^{129}\text{Xe}/^{128}\text{Xe}$  ratio in cliftonite and silicates indicates that the I-Xe system in these samples closed within 2 Ma. Shock is known to disturb the I-Xe system, but it should have affected all types of graphite to a similar degree.

An alternative explanation of  $^{129}\text{Xe}/^{128}\text{Xe}$  ratios in radial rims and platy graphite is the addition of  $^{129}\text{Xe}$  from the low-energy neutron capture reactions on Te:



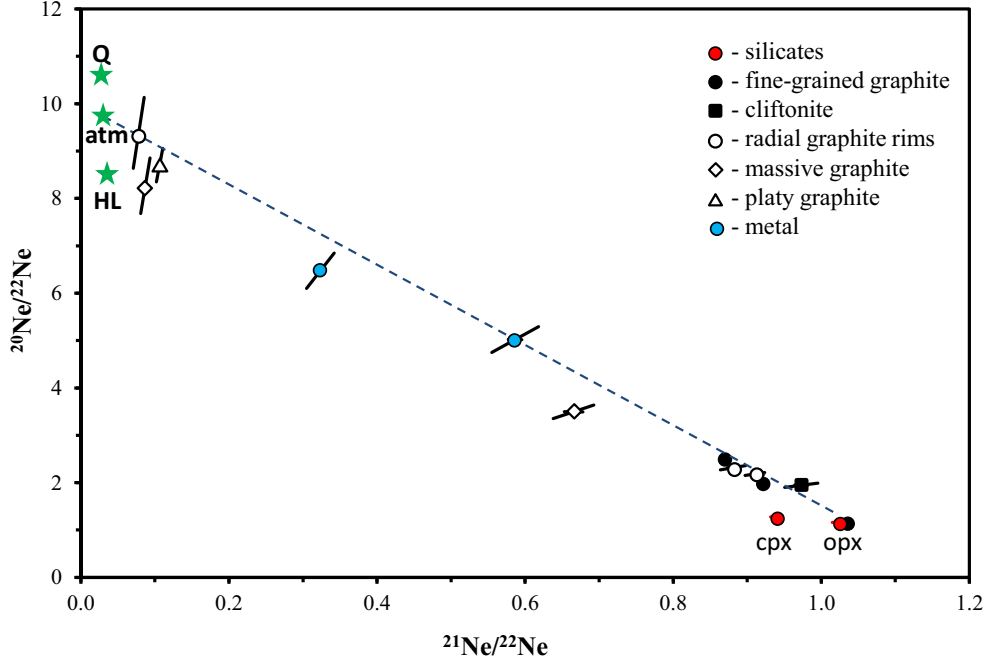
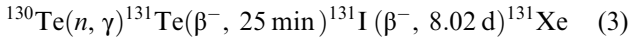


Fig. 6. Neon isotopic composition in the analyzed mineral phases of San Juan A2 is consistent with a mixture of cosmogenic Ne and air. Data points for two massive graphite samples suggest possible contribution from the HL component, characteristic of meteoritic nanodiamonds. Green stars represent various Ne components, error bars are  $1\sigma$ ; opx = orthopyroxene; cpx = clinopyroxene.



Tellurium-derived  $^{129}\text{I}$  subsequently decays ( $T_{1/2} = 15.7 \text{ Ma}$ ) into  $^{129*}\text{Xe}$ , skewing iodine-derived radiogenic  $^{129*}\text{Xe}/^{128*}\text{Xe}$  values in the Te-bearing samples. Neutron captures on  $^{130}\text{Te}$  such as



and



can be used to monitor GCR reactions on Te. Among the samples that show  $^{129*}\text{Xe}$  excesses over the iodine-derived  $^{129}\text{Xe}$ , only one radial graphite rim exhibits slightly higher than 2 sigma  $^{131}\text{Xe}$  excess over the atmospheric value (Fig. 9).  $^{131}\text{Xe}/^{132}\text{Xe}$  ratios in two other rims and in the platy graphite inclusion are atmospheric.  $^{129*}\text{Xe}_{\text{Te}}/^{131*}\text{Xe}_{\text{Te}}$  in troilite from the Cape York iron meteorite was estimated to be about 4, consistent with the epithermal neutron irradiation (Mathew and Marti 2009). Assuming similar neutron spectra for Campo del Cielo,  $^{131*}\text{Xe}_{\text{Te}}$  in the San Juan A2 mineral phases analyzed here is expected to be below the detection limit.

In chondrites, I and Te are strongly correlated and appear to reside in the same phase (Goles and Anders 1962). Troilite is different; it is Te-rich and generally did not incorporate extinct  $^{129}\text{I}$  at the time of formation. That is why troilite was excluded from the noble gas studies in this work. For example, the mean concentration of Te in Canyon Diablo troilite is  $5000 \pm 400 \text{ ppb}$ ; compare to  $62 \pm 8 \text{ ppb}$  for I (Goles and Anders 1962). Thus, for troilite, a contribution of Te-derived  $^{129*}\text{Xe}$  will dominate the radiogenic  $^{129*}\text{Xe}$  inventory. Since troilite is highly abundant in San Juan A2 (Fig. 3), diffusion of Te from troilite into the adjacent mineral phases needs to be considered. A recent study concerning the migration behavior of elements in bcc (body centered cubic) iron metal shows that Te is a slow diffuser and exhibits relatively higher diffusivity when compared to the self-diffusion of iron (Zhang et al. 2020). In silicon, Te mobility is mainly governed by self-diffusion and diffusion of substitutional impurities (Janzén et al. 1982). Hence, it is unlikely that the extra  $^{129*}\text{Xe}$  observed in platy graphite and rim graphite compared to cliftonite is related to a variation in Te mobility in both matrices, Si-rich and iron. Although the Te diffusion coefficient in bcc iron significantly increases in the temperature range of 700–1300 K (Zhang et al. 2020), it should be noted that radial rim graphites from the San Juan mass

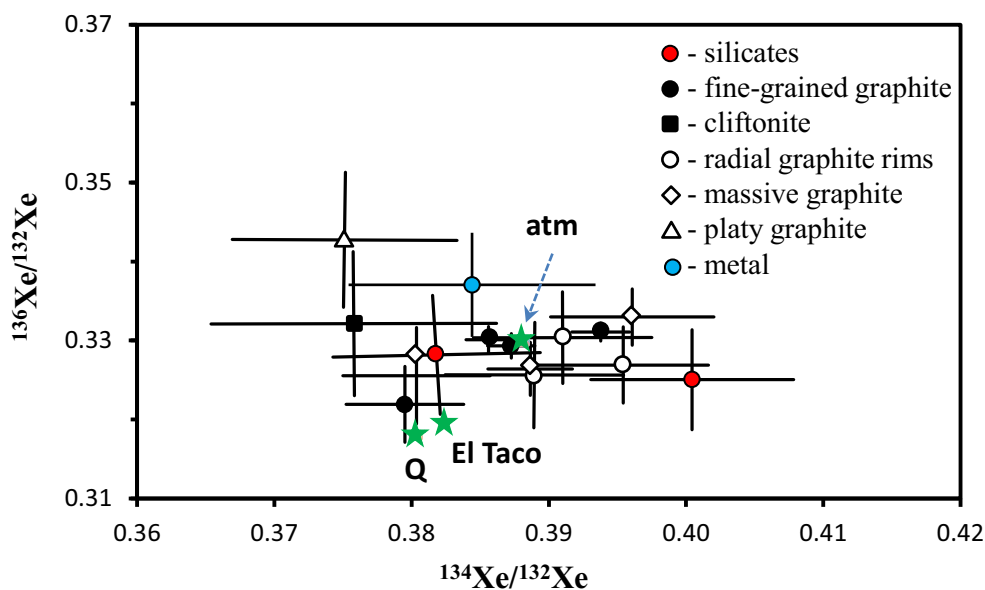


Fig. 7.  $^{136}\text{Xe}/^{132}\text{Xe}$  versus  $^{134}\text{Xe}/^{132}\text{Xe}$  in metal, silicates, and graphite from San Juan A2. Green stars represent trapped components, error bars are  $1\sigma$ . Air Xe is from Ozima and Podosek (1983), Q-Xe is from Busemann et al. (2000), and El Taco Xe id from Mathew and Begemann (1995).

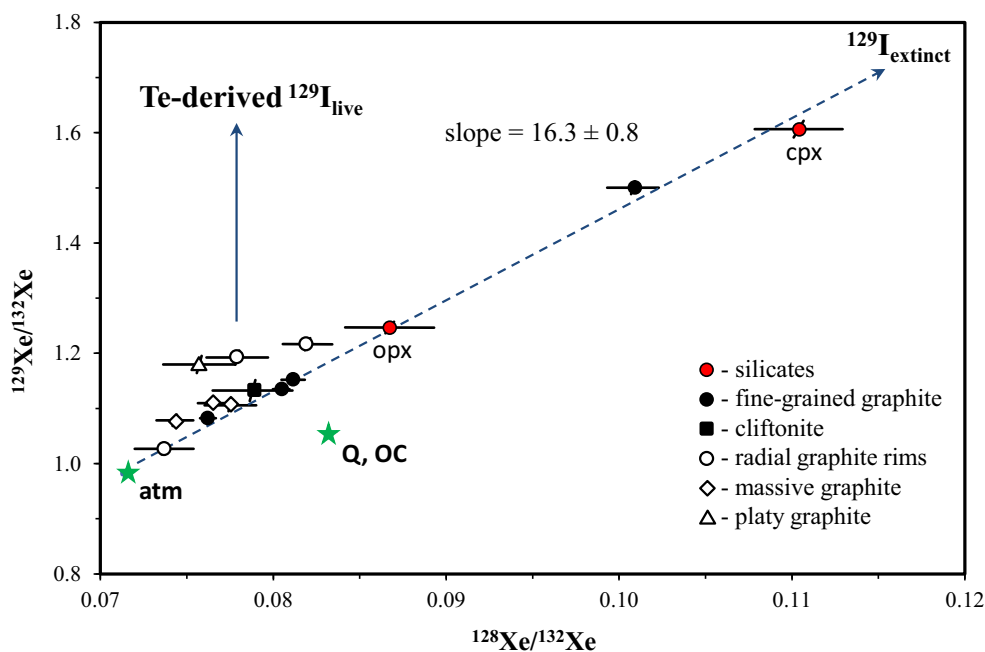


Fig. 8. Xenon three-isotope plot for silicates and graphite from San Juan A2. Xe isotopic composition in metal was atmospheric and is not shown on the plot. I-Xe isochron is defined by solid symbols. Green stars represent various Xe components, error bars are  $1\sigma$ . The linear correlation between  $^{128}\text{Xe}$  and  $^{129}\text{Xe}$  (dashed line) is characteristic of iodine-derived Xe, where the slope of the line depends on the thermal neutron fluence.  $^{129}\text{Xe}$  is a decay product of now extinct  $^{129}\text{I}$  ( $T_{1/2} = 15.7$  Ma).  $^{128}\text{Xe}$  is produced by cosmic ray secondary neutron capture on  $^{127}\text{I}$ .

of Campo del Cielo (IAB) show sub-mm heterogeneity of  $\delta^{13}\text{C}$  values (Maruoka et al. 2003), similar to those found in El Taco IAB iron (Zipfel et al. 1997). This

puts the additional constraints on Te mobility, since C, as a fast diffuser (Gösele 1988), should be affected by the thermal events to a higher degree than Te.

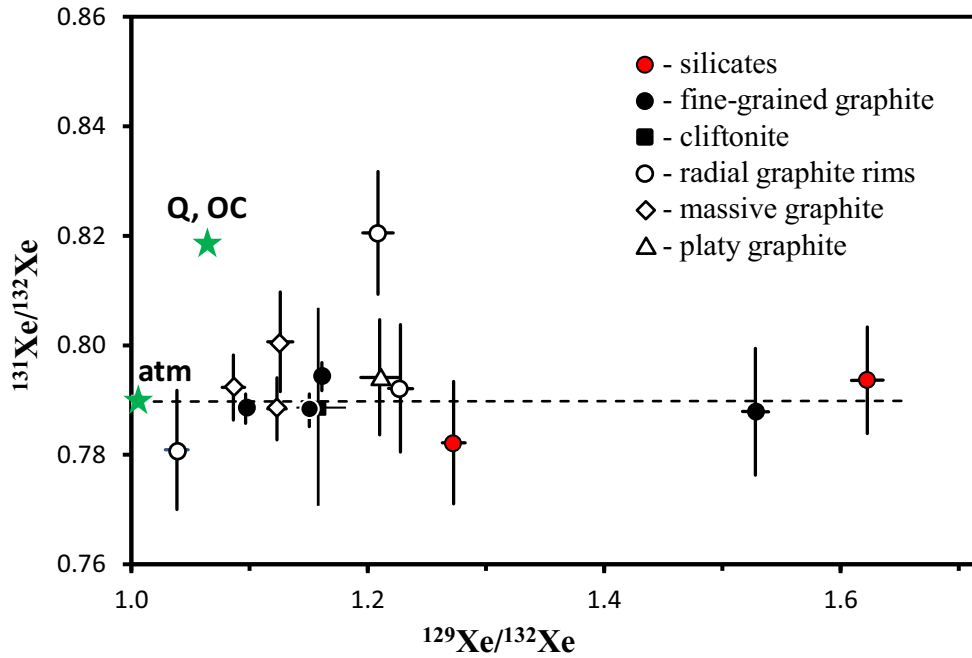


Fig. 9.  $^{131}\text{Xe}/^{132}\text{Xe}$  versus  $^{129}\text{Xe}/^{132}\text{Xe}$  in silicates and graphite from San Juan A2. Isotopic composition of Xe in metal was consistent with air and is not shown on the plot. Green star represents Xe atmospheric composition. Dashed horizontal line defines the atmospheric  $^{131}\text{Xe}/^{132}\text{Xe}$  value.

The reason behind the  $^{129}\text{Xe}$  excesses in the radial rims; platy graphite; and, to a lesser degree, in the massive graphite, is likely more trivial. Analyzed silicates were chosen for their large size and the absence of inclusions, so the rastered areas were well in the middle of silicates and away from the edges. But the radial rims, analyzed here, were 30  $\mu\text{m}$  wide at most, so the adjoining mineral phases, including silicates and troilite, were unavoidably heated during the repeated laser rastering of these areas (Fig. 2). Admixture of radiogenic iodine-derived Xe from silicates would have moved radial rim data points along the correlation line on the three-isotope plot. But contribution from Te-derived  $^{129}\text{Xe}$  would shift experimental points above the isochron (Fig. 8). If only two silicate inclusions had abundant troilite at the edge and thus close to the rim, it could explain why the  $^{129}\text{Xe}$  excess was observed only in two radial rim samples. The platy graphite and the massive graphite rasters covered about  $400 \times 200 \mu\text{m}$ , increasing probability of contribution from the impurities in graphite.

Small excesses on  $^{126}\text{Xe}$  were observed, but only in fine-grained graphites where the largest volumes of material were excavated during the laser rastering. As a result, the  $^{126}\text{Xe}/^{132}\text{Xe}$  ratios were determined with smaller uncertainty, resolving the difference with the atmospheric  $^{126}\text{Xe}/^{132}\text{Xe}$  value. These excesses cannot be explained by interferences and persist independent of the data treatment protocols,  $\sim 6\sigma$  for Fgr2 and  $\sim 4\sigma$  for

Fgr1 (Fig. 10). They are not accompanied by  $^{124}\text{Xe}/^{132}\text{Xe}$  enrichment, as expected in the case of spallation. To explain such  $^{126}\text{Xe}$  enrichments observed in some meteorites and lunar soils, Pepin et al. (1995) discussed neutron- and solar proton-induced reactions on  $^{127}\text{I}$ , while Begemann and Mathew (1996) suggested solar proton reactions on Te. Both scenarios require regolith irradiation. The production rate ratios for low-energy proton-induced reactions on Te were estimated to be  $P(^{128}\text{Xe})/P(^{126}\text{Xe}) = 1.42$  and  $P(^{130}\text{Xe})/P(^{126}\text{Xe}) = 0.33$  (Begemann and Mathew 1996). In the case of San Juan,  $^{128}\text{Xe}$  enrichments due to (p,xn) reactions on Te would be masked by more abundant  $^{128}\text{Xe}$  produced by neutron capture on  $^{127}\text{I}$ . When presented as  $^{130}\text{Xe}/^{132}\text{Xe}$  versus  $^{126}\text{Xe}/^{132}\text{Xe}$  (Fig. 10), data points for San Juan suggest a correlation between  $^{130}\text{Xe}$  and  $^{126}\text{Xe}$ , although  $^{130}\text{Xe}/^{132}\text{Xe}$  ratios are effectively atmospheric within uncertainties, as is expected from  $P(^{130}\text{Xe})/P(^{126}\text{Xe}) = 0.33$  production rates ratio for low-energy proton-induced reactions on Te. Nevertheless, no  $^{126}\text{Xe}$  enrichment was observed in radial rims, platy and massive graphite samples where the excesses due to low-energy neutron captures on Te are evident. Instead,  $^{126}\text{Xe}/^{132}\text{Xe}$  ratio in orthopyroxene is above the atmospheric value, although within the uncertainty. To summarize, the observed  $^{126}\text{Xe}$  excesses are intriguing and appear to be supported by  $^{130}\text{Xe}$  data, but the effects are too small here to draw a conclusion on their nature.

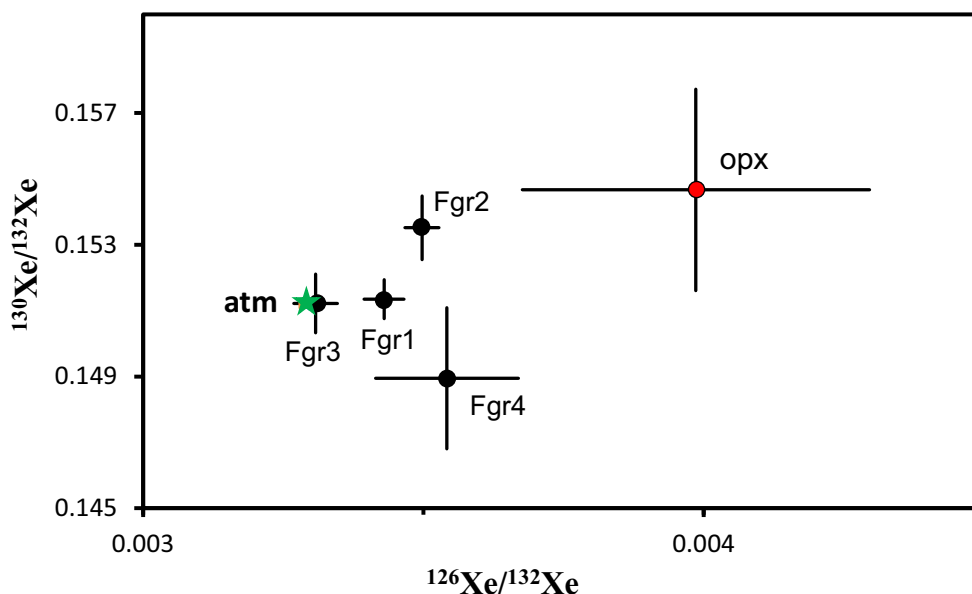


Fig. 10.  $^{130}\text{Xe}/^{132}\text{Xe}$  versus  $^{126}\text{Xe}/^{132}\text{Xe}$  in fine-grained graphite and orthopyroxene. Data points for other graphite samples and clinopyroxene are atmospheric within  $2\sigma$  and are not shown for clarity. Green star represents air, errors are  $1\sigma$ .

## CONCLUSIONS

The petrographic study of the San Juan A2 polished section demonstrated textural and compositional similarities with the Campo del Cielo IAB iron meteorite, with trace element abundances in metal following exactly the pattern of bulk Campo del Cielo (Jochum et al. 1980; Hoashi et al. 1993; Choi et al. 1995).

Ratios of spallogenic He and Ne isotopes follow the correlation trend defined by the published data for iron meteorites where  $^3\text{He}/^4\text{He}$  values decrease and  $^4\text{He}/^{21}\text{Ne}$  values increase with the size of meteorite. Data points for San Juan metal are similar to the values reported for the El Taco fragment of Campo del Cielo (Nyquist et al. 1967). Based on the Ne isotopic composition of its components, and the observed correlation between  $^{128}\text{Xe}$  and  $^{129}\text{Xe}$ , the San Juan A fragment of Campo del Cielo was well shielded from primary high-energy cosmic ray irradiation. Its size allowed the secondary neutrons to be fairly well thermalized. As a result, in 180 Ma of a simple single-stage irradiation with constant exposure geometry (Honda et al. 2009), Campo del Cielo received an equivalent (normalized to the MURR spectrum) fluence of thermal and epithermal neutrons of  $6.6 \times 10^{17} \text{ n cm}^{-2}$ . Assuming the neutron spectra are identical for MURR and Campo del Cielo, the average thermal equivalent neutron flux for these fragments is about  $1.2 \times 10^2 \text{ n cm}^{-2} \text{ s}^{-1}$ . Xe isotopic composition in the radial graphite rims and platy graphite shows evidence of live  $^{129}\text{I}$  in San Juan

and is consistent with a mixture of radiogenic I-derived and Te-derived Xe.

*Acknowledgments*—The authors share warm memories of John Wasson. His encouragement and many stimulating conversations helped to increase our knowledge on Campo del Cielo. We thank Dr. Kattathu Mathew and an anonymous reviewer for the constructive comments and suggestions. This work was supported by NASA grant 80NSSC19K0508 to O.P. and PICT 1562 (Agencia-MINCyT) to M.E.V. The software for laser ablation and for the noble gas analyses was written by John Stehman.

*DATA AVAILABILITY STATEMENT*—The data that support the findings of this study are provided in the manuscript. Additional data are available on request from the corresponding author.

*Editorial Handling*—Dr. Edward Scott

## REFERENCES

- Basford J. R., Dragon J. C., Pepin R. O., Coscio M. R. Jr., and Murthy V. R. 1973. Krypton and xenon in lunar fines. Proceedings, 4th Lunar Science Conference. pp. 1915–1955.
- Begemann F. and Mathew K. J. 1996. On the production by solar protons of  $^{126}\text{Xe}$  via Te (p, xn) reactions. *Geochimica et Cosmochimica Acta* 60:4593–4597.
- Benedix G. K., McCoy T. J., Keil K., and Love S. G. 2000. A petrologic study of the IAB iron meteorites: Constraints

- on the formation of the IAB-winnonaite parent body. *Meteoritics & Planetary Science* 35:1127–1141.
- Bogard D. D., Nyquist L. E., Bansal B. M., Garrison D. H., Wiesmann H., Herzog G. F., Albrecht A. A., Vogt S., and Klein J. 1995. Neutron-capture  $^{36}\text{Cl}$ ,  $^{41}\text{Ca}$ ,  $^{36}\text{Ar}$ , and  $^{150}\text{Sm}$  in large chondrites: Evidence for high fluences of thermalized neutrons. *Journal of Geophysical Research* 100:9401–9416.
- Bogard D. D., Garrison D. H., and Takeda H. 2005. Ar-Ar and I-Xe ages and the thermal history of IAB meteorites. *Meteoritics & Planetary Science* 40:207–224.
- Burnett D. S., Huneke J. C., Podosek F. A., Russ G. P. III, Turner G., and Wasserburg G. J. 1972. The irradiation history of lunar samples. Proceedings, 3rd Lunar Science Conference. pp. 105–107.
- Busemann G., Baur H., and Wieler R. 2000. Primordial noble gases in “phase Q” in carbonaceous and ordinary chondrites studied by closed-system stepped etching. *Meteoritics & Planetary Science* 35:949–973.
- Campbell A. J., Humayun M., Meibon A., Krot A., and Keil K. 2001. Origin of the zoned metal grains in the QUE94411 chondrite. *Geochimica et Cosmochimica Acta* 65:163–180.
- Choi B., Ouyang X., and Wasson J. 1995. Classification and origin of IAB and III CD iron meteorites. *Geochimica et Cosmochimica Acta* 59:593–612.
- Curtis D. B. and Wasserburg G. J. 1975. Processes of sedimentation and mixing in the lunar regolith inferred from neutron fluence measurements. Proceedings, 6th Lunar Science Conference. pp. 172–174.
- Göbel R., Ott U., and Begemann F. 1978. On trapped noble gases in ureilites. *Journal of Geophysical Research* 83:855–867.
- Göbel R., Begemann F., and Ott U. 1982. On neutron-induced and other noble gases in Allende inclusions. *Geochimica et Cosmochimica Acta* 46:1777–1792.
- Goles G. G. and Anders E. 1962. Abundance of iodine tellurium and uranium in meteorites. *Geochimica et Cosmochimica Acta* 26:723–737.
- Gösele U. M. 1988. Fast diffusion in semiconductors. *Annual Review of Materials Research* 18:257–282.
- Hintenberger H. and Wänke H. 1963. Helium and neon isotope in Eisenmeteoriten. *Zeitschrift für Naturforschung* 19a:210–218.
- Hoashi M., Brooks R. R., and Reeves R. D. 1993. Palladium, platinum and ruthenium in iron meteorites and their taxonomic significance. *Chemical Geology* 106:207–218.
- Honda M., Nagai H., Nagao K., Bajo K., Takaoka N., Oura Y., and Nishizumi K. 2009. Irradiation histories of iron meteorites. *Journal of the Physical Society of Japan* 78:12–17.
- Huss G. R. and Lewis R. S. 1994. Noble gases in presolar diamonds I: Three distinct components and their implications for diamonds origins. *Meteoritics & Planetary Science* 29:7915–8810.
- Janzén E., Grimmeiss H. G., Lodding A., and Deline C. H. 1982. Diffusion of tellurium dopant in silicon. *Journal of Applied Physics* 53:7367–7671.
- Jochum K. P., Seufert M., and Begemann F. 1980. On the distribution of major and trace elements between metal and phosphide phases of some iron meteorites. *Zeitschrift für Naturforschung* 35a:57–63.
- Kracher A. 1982. Crystallization of a S-saturated Fe, Ni-melt, and the origin of iron meteorite groups IAB and III CD. *Geophysical Research Letters* 9:412–415.
- Kurat G., Varela M. E., Ametrano S. J., and Brandstätter F. 2002. Major, minor and trace element abundances in metal and schreibersite of the San Juan A mass of Campo Del Cielo (IAB) (abstract #1781). 33rd Lunar and Planetary Science Conference. CD-ROM.
- Lavielle B., Marti K., Jeannot J.-P., Nishiizumi K., and Caffee M. 1999. The  $^{36}\text{Cl}$ - $^{36}\text{Ar}$ - $^{40}\text{K}$ - $^{41}\text{K}$  records and cosmic ray production rates in iron meteorites. *Earth and Planetary Science Letters* 170:93–104.
- Liberman R. G., Fernández N. J. O., di Tada M. L., Fifield L. K., Masarik J., and Reedy R. C. 2002. Campo del Cielo iron meteorite: Sample shielding and meteoroid’s preatmospheric size. *Meteoritics & Planetary Science* 37:295–300.
- Lodders K., Palme H., and Gail H.-P. 2009. Abundances of the elements in the solar system. In *Solar system, Landolf-Börnstein—Group VI astronomy and astrophysics*, volume 4B, edited by Trümper, J. E. Berlin: Springer-Verlag. pp. 560–630.
- Maruoka T., Matsuda J., and Kurat G. 2001. Abundance and isotopic composition of noble gases in metal and graphite of the Bohumitz IAB iron meteorite. *Meteoritics & Planetary Science* 36:597–609.
- Maruoka T., Kurat G., Zinner E., Varela M. E., and Ametrano S. 2003. Carbon isotopic heterogeneity of graphite in the San Juan mass of Campo del Cielo IAB iron meteorite (abstract #1663). 36th Lunar and Planetary Science Conference. CD-ROM.
- Mathew K. J. and Begemann F. 1995. Isotopic composition of xenon and krypton in silicate-graphite inclusions of the El Taco, Campo del Cielo, IAB iron meteorite. *Geochimica et Cosmochimica Acta* 59:4729–4746.
- Mathew K. J. and Marti K. 2009. Galactic cosmic ray-produced  $^{129}\text{Xe}$  and  $^{131}\text{Xe}$  excesses in troilites of the Cape York iron meteorite. *Meteoritics & Planetary Science* 44:107–114.
- Meshik A. and Pravdivtseva O. 2016. Noble gas laboratory at Washington University: History and analytical capabilities (abstract #1681). 47th Lunar and Planetary Science Conference. CD-ROM.
- Niemeyer S. 1979. I-Xe dating of silicate and troilite from IAB meteorites. *Geochimica et Cosmochimica Acta* 43:843–860.
- Nyquist L. E., Huneke J. C., and Signer P. 1967. Spallogenic rare gases in the El Taco meteorite. *Earth and Planetary Science Letters* 2:241–248.
- Ozima M. and Podosek F. A. 1983. *Noble gas geochemistry*. Cambridge: Cambridge University Press. 367 p.
- Pepin R. O., Becker R. H., and Rider P. E. 1995. Xenon and krypton isotopes in extraterrestrial regolith soils and in the solar wind. *Geochimica et Cosmochimica Acta* 59:4997–5022.
- Podosek F. A. 1970. Dating of meteorites by the high-temperature release of iodine-correlated  $^{129}\text{Xe}$ . *Geochimica et Cosmochimica Acta* 34:341–366.
- Pravdivtseva O., Meshik A., Hohenberg C. M., and Kurat G. 2013. I-Xe ages of Campo del Cielo silicates as a record of the complex early history of the IAB parent body. *Meteoritics & Planetary Science* 48:2480–2490.
- Pravdivtseva O., Tissot F. L. H., Dauphas N., and Amari S. 2020. Evidence of presolar SiC in the Allende Curious Marie calcium-aluminum-rich inclusion. *Nature Astronomy* 4:617–624.
- Ruzicka A. 2014. Silicate-bearing iron meteorites and their implications for the evolution of asteroidal parent bodies. *Chemie der Erde* 74:3–48.
- Takeda H., Bogard D. D., Mittlefehldt D. W., and Garrison D. H. 2000. Mineralogy, petrology, chemistry, and

- $^{39}\text{Ar}$ - $^{40}\text{Ar}$  and exposure ages of the Caddo County IAB iron: Evidence for early partial melt segregation of a gabbro area rich in plagioclase-diopside. *Geochimica et Cosmochimica Acta* 64:1311–1327.
- Vogel N. and Renne P. R. 2008.  $^{40}\text{Ar}$ - $^{39}\text{Ar}$  dating of plagioclase grain size separates from silicate inclusions in IAB iron meteorites and implications for the thermochronological evolution of the IAB parent body. *Geochimica et Cosmochimica Acta* 72:1231–1255.
- Voshage H., Feldmann H., and Braun O. 1983. Investigations of cosmic-ray-produced nuclides in iron meteorites: 5. More data on the nuclides of potassium and noble gases, on exposure ages and meteoroid sizes. *Zeitschrift für Naturforschung* 38a:273–280.
- Wasson J. T. and Kallemeyn G. W. 2002. The IAB iron-meteorite complex: A group, five subgroups, numerous grouplets, closely related, mainly formed by crystal segregation in rapidly cooling melts. *Geochimica et Cosmochimica Acta* 66:2445–2473.
- Wasson J. T., Willis J., Wai C. M., and Kracher A. 1980. Origin of iron meteorite groups IAB and IIICD. *Zeitschrift für Naturforschung* 35a:781–795.
- Wlotzka F. and Jarosewich E. 1977. Mineralogical and chemical compositions of silicate inclusions in the El Taco, Camp del Cielo, iron meteorite. *Smithsonian Contributions to the Earth Sciences* 19:104–125.
- Zhang Z.-D., Ren C.-L., Tan M.-L., Yang Y.-Q., Yin Y.-R., Wang C.-Y., Han H., and Huai P. 2020. Migration behavior of tellurium in bcc iron against typical alloying elements: A first-principles study. *Computational Materials Science* 181:109571.
- Zipfel J., Hutcheon I. D., and Marti K. 1997. Carbon isotopic composition of graphite in the El Taco IAB iron meteorite (abstract #1707). 28th Lunar and Planetary Science Conference. CD-ROM.
-